# Breaking Crystallinity for Optimal Dark Current: Nonfullerene Acceptor Dilution as a Strategy for High-Performance Organic Photodetectors

*Chiara Labanti, Ying Sun, Joel Luke, Yifan Dong, Song Yi Park, Yi-Chun Chin, Tianhao Lan, Emily J. Yang, Lei Zhang, Soranyel Gonzalez-Carrero, James R. Durrant, and Ji-Seon Kim\**

Organic photodetectors (OPDs) based on polymer donor:non-fullerene-acceptor (NFA) bulk heterojunction (BHJ) blends demonstrate great potential for light-sensing applications, thanks to optoelectronic tunability and strong absorption. However, state-of-the-art organic photoconversion devices lag behind silicon counterparts due to the laborious dark current, $J_d$, and photodetection speed optimization required in OPDs. Herein, the donor/acceptor blend ratio is controlled to optimize PM6:Y6-based OPDs, with diluted Y6 blends (1:0.1 D/A weight ratio) strongly suppressing $J_d$ to $6.5 \times 10^{-9}$ A cm$^{-2}$ ($-4$ V). Diluted OPDs exhibit faster photoresponse and poor short-circuit photocurrent generation is dramatically improved under reverse bias. In-depth photophysical and energetic analysis reveal the origin of high performance. In diluted blends, dissociation of emissive strongly bound excitonic charge-transfer states within Y6 require electric field assistance, while the polymer matrix provides a continuous charge-transport pathway. The generality of this strategy is tested with various NFAs, with NFA dilution being most effective for highly crystalline acceptors. It is determined that the reduction in dark current is predominantly driven by disruption of NFA crystallinity and intermolecular interactions. Polymer-rich BHJ devices, therefore, provide an effective optimization method for reducing dark current in OPDs and are highly promising for industrial scalability due to facile processability, robust mechanical properties, and superior thermal stability.

## 1. Introduction

Recent years have witnessed impressive technological advancement in organic optoelectronics, with organic semiconductors such as polymers and small molecules demonstrating steady performance increase in a multitude of device applications.[1–4] Organic photodetectors (OPDs), in particular, are very promising for a wide range of applications, including optical communication, large-area imagers, machine vision, and wearable sensors.[5,6] Here, the development of non-fullerene acceptors (NFAs) has benefited OPD progress enabling tunable energetics, strong visible-infrared absorption, adaptability to match a wide variety of donor materials, attractive mechanical properties (lightweight, flexibility), and low-cost solution-based processing.[7–9]

To further boost OPD device performance both materials design and photoactive layer engineering must be carefully considered. In particular, the exciton dissociation process via intermediate charge-transfer (CT) states should

C. Labanti[+], Y. Sun, J. Luke, S. Y. Park, Y.-C. Chin, T. Lan, E. J. Yang, L. Zhang, J.-S. Kim
Department of Physics and Centre for Processable Electronics
Imperial College London
Blackett Laboratory
London SW7 2AZ, UK
E-mail: ji-seon.kim@imperial.ac.uk

The ORCID identification number(s) for the author(s) of this article can be found under https://doi.org/10.1002/adom.202500255

[+]Present address: Graduate Institute of Photonics and Optoelectronics and Department of Electrical Engineering, National Taiwan University, Taipei 10617, Taiwan

J. Luke
Physical Sciences and Engineering Division (PSE)
King Abdullah University of Science and Technology (KAUST)
Thuwal 23955-6900, Saudi Arabia

Y. Dong, S. Gonzalez-Carrero, J. R. Durrant
Department of Chemistry and Centre for Processable Electronics
Imperial College London
Molecular Sciences Research Hub
White City Campus, London W12 0BZ, UK

Y. Dong
Chemistry and Nanoscience Center
National Renewable Energy Laboratory
Golden, CO 80401, USA

S. Y. Park
Department of Physics
Pukyong National University
Busan 48513, Republic of Korea

**ADVANCED
SCIENCE NEWS**

www.advancedsciencenews.com

**ADVANCED
OPTICAL
MATERIALS**

www.advopticalmat.de

be optimized.[9,10] In bulk heterojunctions (BHJs), this occurs at the donor(D)/acceptor(A) interface, driven by the energy offsets between the highest occupied molecular orbital (HOMO) and lowest unoccupied molecular orbital (LUMO) levels, and by the external electric field applied during OPD operation.

In terms of materials design, the emergence of the fused benzothiadiazole-core-based Y6 family of acceptors has marked a turning point for the NFA field, showing record-breaking device efficiency in organic photovoltaics (OPVs).[11–13] The unique photophysical properties of Y6 () are due to its beneficial molecular characteristics (A–D–A'–D–A calamitic structure,[14] high quadrupole moment,[15,16] strong $\pi$-$\pi$ stacking),[17] leading to efficient charge dissociation, and low voltage losses.[18] In particular, strong band bending at domain interfaces by quadrupole-induced electrostatic interactions has been shown to contribute to efficient charge generation even in single-component Y6 systems.[14,19–21] However, the application of Y6 in OPDs is more limited, due to large BHJ domain segregation leading to small D/A interfacial areas which are undesirable for photocurrent generation under OPD operation. In addition, the small bandgap and broad absorption spectrum of Y6 are not always preferable, particularly for narrowband photodetection.[22–25] In order to improve device performance further and realize the potential of Y6 for OPD applications, it is necessary to enhance photocurrent generation, suppress dark current, and achieve narrowband photodetection.

Dark current density ($J_d$), which is the current generated under reverse bias without any light excitation is an important metric that contributes to the performance of different photoconversion devices such as low-light photovoltaics,[26] and is a key figure of merit (FOM) in defining OPD performance. Dark current is typically traced back to the dark injection from the contacts and, to a lesser extent, the thermal generation of electron-hole pairs.[5] Detailed understanding of $J_d$ origin and strategies to minimize it are still the subject of ongoing research. For example, it has been shown that $J_d$ scales with device open-circuit voltage $V_{OC}$ as the diode dark saturation current $J_0$ is given by:

$$J_o \approx J_{SC} \exp\left(-\frac{qV_{OC}}{k_B T}\right) \tag{1}$$

which is valid for $V_{OC} \gg k_B T/q$, where $J_{SC}$ is the short-circuit current, $k_B$ is the Boltzmann constant, $T$ the temperature of the system and $q$ the elementary charge.[6] Low $J_d$ thus requires a high $V_{OC}$, which can be manipulated by HOMO/LUMO tuning towards high CT state energy ($E_{CT}$) or by D/A interface engineering.[27,28] However, other factors contribute to $J_d$, such as energetic disorder at the semiconductor band-edge, trap-assisted charge generation, and incomplete contacts at the electrodes.[5,29]

In these regards, the prototypical PM6:Y6 system shows favorable characteristics, such as narrow tail-state distribution and extremely low trap density.[18] OPDs also require fast photoresponse times, which are related to continuous percolation pathways in BHJ and good charge transport of the D and A species.[5]

One approach to optimize these properties is by engineering of the photoactive layer, with one important parameter being the D/A blend ratio. This approach is desirable because it doesn't require additional fabrication steps, unlike sequentially deposited donor and acceptor layers.[24] While balanced D/A proportions are preferred in OPVs for ideal domain size, blend ratio tuning can induce interesting effects on the BHJ photophysics.[30] For example, an increase in $V_{OC}$ for PM6:Y6 OPVs with higher PM6 content has been ascribed to a higher $E_{CT}$.[31] Typically, however, a higher Y6 content is used as it yields better OPV power conversion efficiencies (PCEs).[32,33] In fullerene-based systems, blend ratio engineering has been used to modify the $E_{CT}$ to enhance $V_{OC}$ through control of the D and A morphology to impact interfacial energetics.[34,35] Other reports, suggest that blend ratio engineering can enhance $V_{OC}$ independently of $E_{CT}$ by reducing the D/A interfacial area, which suppresses bimolecular recombination losses.[27] The effect of D/A blending ratio on $V_{OC}$ offers an opportunity to regulate dark current Equation (1) for improving OPD performance. However, this approach has received limited attention in polymer:NFA BHJs, and detailed studies on solution-processed systems are still needed.

We note that blend ratio control has successfully been used to alter the working mechanism of OPDs. In literature, highly diluted (e.g., D:A, 100:1) systems are used to activate a photomultiplication (PM-OPDs) regime in which EQEs can exceed 100%.[36] Despite the large detectivities enabled through this mechanism, the response time of PM-OPDs are slow (usually milliseconds), thus being unsuitable for high-speed photodetection.[37] Our method focuses on improving the dark current of photodiode OPDs, which allows us to achieve excellent detectivity while maintaining microsecond response times.

In this work, we demonstrate highly efficient solution-processed OPDs using a highly diluted blend of Y6 in a PM6 polymer donor matrix (i.e., "diluted" BHJ with a 1:0.1 D/A weight ratio, compared to a "balanced" 1:1.2 blend). The diluted blend has a suppressed $J_d$ of $10^{-9}$ A cm$^{-2}$, and sufficient responsivity under reverse bias is maintained despite the limited D/A interface area, resulting in an excellent specific detectivity of $5 \times 10^{12}$ Jones. Together with the faster photodetection (i.e., < 4.5 µs fall times), polymer donor-rich devices show record FOMs among state-of-the-art solution-processed BHJ OPDs.[25,38–41] By detailed electric-field-dependent optoelectronic characterization and transient spectroscopy, we identify the origin of superior OPD performance in diluted blends. This surmounts to three key factors: 1) effective dissociation under reverse electric field of bound Y6 charge transfer excitonic (CTE) states in the diluted blends; 2) a continuous polymer percolation network for fast photoresponse; and 3) a favorable energetic landscape that prevents dark charge injection and thermal generation, reducing $J_d$. Furthermore, by implementing the dilution strategy for a range of D/A BHJ blends, we demonstrate the generality of this approach for lowering dark current and enhancing OPD performance. These results show that polymer-rich BHJ devices are very promising as high-performance OPDs and should be

J. R. Durrant
Department of Materials Science and Engineering
University of Swansea
Swansea SA1 8EN, UK

J.-S. Kim
Department of Chemistry
University of Oxford
Oxford OX1 3TA, UK
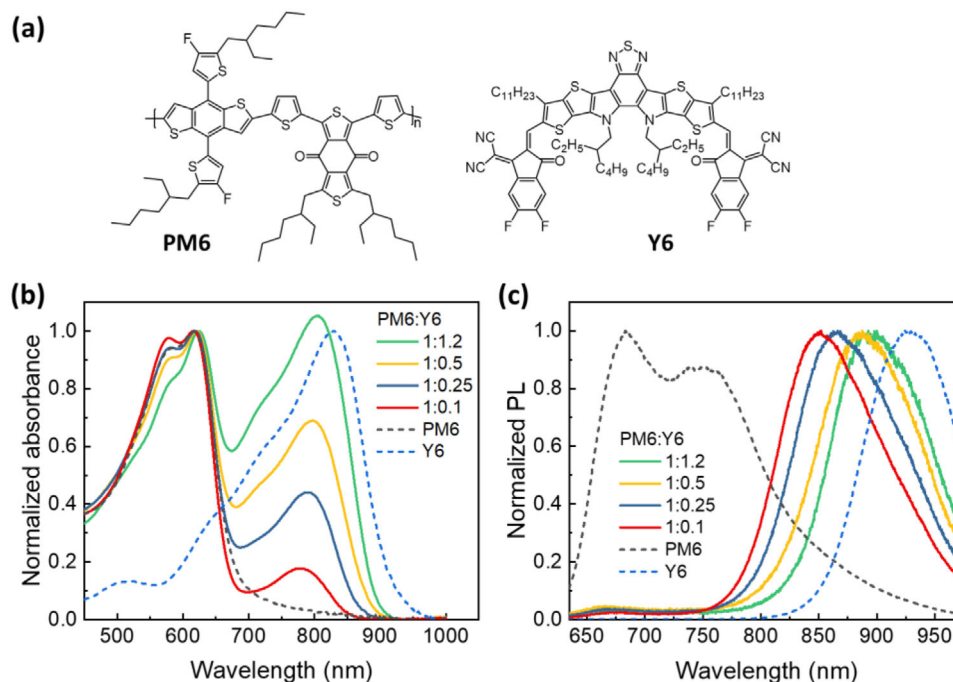
**Figure 1.** Optical properties of PM6:Y6 blends with different D/A blend ratios. a) Molecular structures of PM6 and Y6. b) UV–Vis absorbance, normalized to the PM6 0-0 peak. c) Photoluminescence spectra, normalized to main emission of PM6 or Y6.

considered for industrially-relevant applications due to facile processability, with the polymer-rich system having the added benefits of good thermal stability and appealing mechanical properties.[42–45]
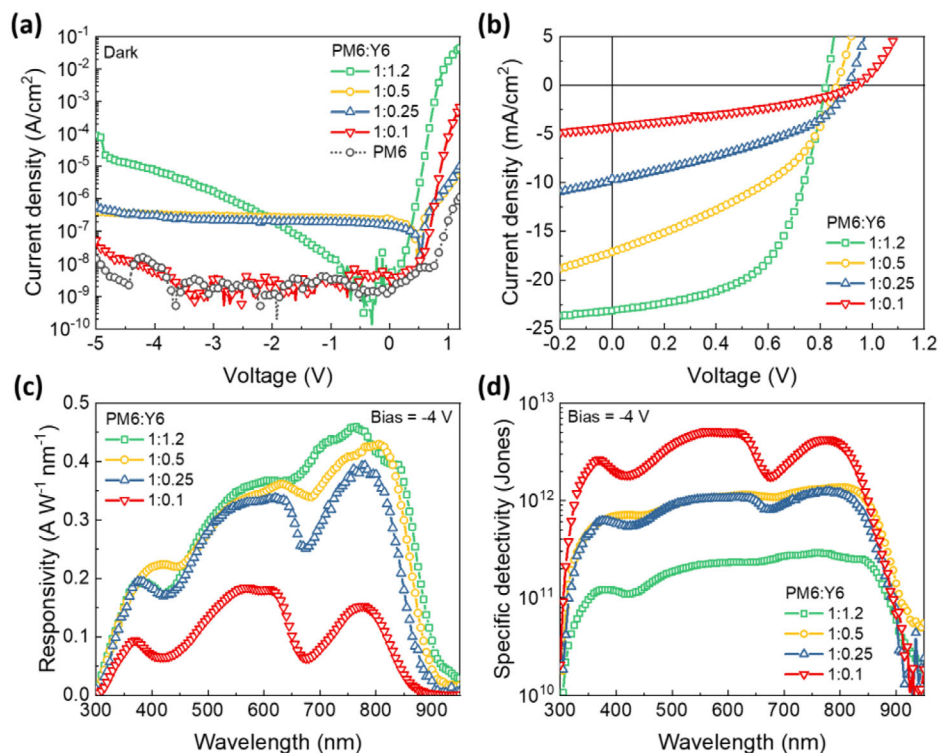
## 2. Results and Discussion

### 2.1. Impact of Acceptor Dilution on Optoelectronic Properties

First, we compare optical properties of PM6:Y6 BHJs with various D/A ratios by progressive dilution of the acceptor (see molecular structure of PM6 and Y6 in **Figure 1a**). Absorption and photoluminescence (PL) spectra of neat and BHJ films are shown in Figure 1b,c, respectively. A full series of data with and without normalization are shown in Figure S1 (Supporting Information) (absorption) and Figure S2 (Supporting Information) (PL). As apparent from the UV–vis spectra, increasing PM6 content shifts the Y6 absorption to higher energies (from 830 nm of neat Y6 to 780 nm for 1:0.1 dilution). This indicates a disruption of the Y6 crystallinity as the polymer donor content is increased. At the same time, the 0–1 absorption peak of PM6 around 575 nm is enhanced for higher PM6 content, which is related to an increase in H-aggregation between polymer chains.[46] In the PL spectra, Y6 dilution in PM6 results in an even stronger blue-shift, with over 75 nm difference between the neat acceptor and the diluted BHJ films (i.e., 1:0.1 weight ratio). As this Y6 emission shifts to higher energy upon dilution the absolute intensity of emission increases despite the lower Y6 content (Figure S2c, Supporting Information), indicating less Y6 aggregation-induced PL quenching. This emission originates from Y6 rather than the interfacial CT state at the PM6/Y6 interface.[47] The blue-shifted excitonic

emission has previously been assigned to molecular Y6,[48] however, we note that even in our most diluted BHJ films the emission peak (850 nm) is significantly red-shifted relative to molecular Y6 emission in dilute CF solution (817 nm, Figure S2b, Supporting Information). This suggests, that even in diluted blends Y6 molecules are strongly interacting with each other due to their strong D-A character, leading to emissive intermolecular CTE states localized to Y6 domains.[21] This is not to be confused with the interfacial CT-state at the PM6/Y6 interface, the emission of which we do not observe.[48] Even so, the study by Cheng et al. clearly correlates the blue shift of Y6 emission with a reduction of Y6 crystallinity, as measured using grazing incidence wide angle X-ray scattering, supporting our claim that Y6 crystallinity is disrupted upon dilution.[48] Meanwhile, the emission of PM6 in the 650–800 nm region is almost completely quenched even in the most diluted blend, with the majority of PL arising from the acceptor CTE state. This indicates efficient energy transfer from PM6 to Y6 upon photoexcited exciton formation.[19]

### 2.2. Impact of Acceptor Dilution on Photodetector Performance

PM6:Y6 OPDs with various blend ratios are characterized, using an ITO/ZnO/BHJ/MoO$_3$/Ag device structure, and results are shown in **Figure 2** (full blend ratio series, including neat polymer in Figure S3, Supporting Information). Dark current density–voltage ($J$–$V$) characteristics (Figure 2a) reveal a strongly suppressed $J_d$ at reverse bias for higher polymer content devices. At −4 V, $J_d$ reaches $6.5 \times 10^{-9}$ A cm$^{-2}$ for diluted (1:0.1) devices, compared to $8 \times 10^{-6}$ A cm$^{-2}$ for the balanced case. This dark current improvement, even at high reverse bias, distinguishes

**ADVANCED**
**SCIENCE NEWS**

www.advancedsciencenews.com

**ADVANCED**
**OPTICAL**
**MATERIALS**

www.advopticalmat.de

**Figure 2.** Device characterization for PM6:Y6 active layer with increasing donor content. $J$–$V$ curves in a) dark and b) illuminated (AM1.5G) conditions, c) responsivity at −4 V and d) specific detectivity at −4 V.

our method from others such as sequential deposition, which only reduce dark current significantly without an applied reverse bias.[24] Neat PM6 devices also show excellent $J_d$ levels of $8.4 \times 10^{-9}$ A cm$^{-2}$ at −4 V, suggesting that the high $J_d$ in the balanced blend is predominately driven by Y6. We note that despite this low dark current, PM6 only devices are not suitable for OPD applications due to their inefficient charge generation under illumination (Figure S3c, Supporting Information). Neat Y6 devices also show lower detectivity compared to BHJ devices, due to their increasing dark current with reverse bias, and less efficient current generation under illumination (Figure S4, Supporting Information).

When characterized as OPVs under 1 Sun illumination ($J$–$V$ curves in Figure 2b and summary of PV parameters in Figure S5, Supporting Information) optimal performance is seen in the balanced blends. The higher $J_{SC}$ and FF of these devices being driven by more efficient photocurrent generation under 1 Sun illumination. The higher D/A interfacial area and well-intermixed morphology of balanced blends enables more efficient charge generation, and light harvesting. However, a systematic increase in $V_{OC}$ is observed upon Y6 dilution, from 0.82 V in the balanced device to 1.03 V for the 1:0.05 device, approaching the intrinsic $V_{OC}$ of neat PM6 devices (1.12 V). $V_{OC}$ is strongly related to interfacial CT-state energy and recombination-based $V_{OC}$ losses, including both radiative and nonradiative processes, as detailed below.[27,49,50]

$$V_{oc} = \frac{E_{CT}}{q} - \Delta V_{rad} - \Delta V_{nr} \qquad (2)$$

where $E_{CT}$ is the energy of the interfacial CT-state, $\Delta V_{rad}$ and $\Delta V_{nr}$ are the radiative and nonradiative recombination-based open-circuit voltage losses, respectively. We also measured the light intensity dependent $V_{OC}$ and $J_{SC}$ of both the balanced and diluted devices to investigate the role of recombination on $V_{OC}$ (Figure S6, Supporting Information). The slope of $V_{OC}$ versus ln(light intensity) reflects differences in recombination mechanisms. If the ideality factor $n$, derived from the slope $kT/q$, equals 1, bimolecular recombination dominates; if $n = 2$, trap-assisted recombination is the primary mechanism.[51] Both blends exhibit predominantly bimolecular recombination behavior ($n = 1.00$ for the 1:0.1 blend and $n = 1.03$ for the 1:1.2 blend). $J_{SC}$ follows a power-law relationship with light intensity, i.e., $J_{SC} \propto I_{light}^{\alpha}$, where $\alpha = 1$ for ideal devices, and $\alpha < 1$ when bimolecular recombination occurs.[52] The diluted blend shows a lower gradient of $J_{SC}$ as a function of light intensity compared with the balanced blend. This indicates that recombination is similar in both blends, although bimolecular recombination may be more significant in diluted blends and, therefore, does not explain the improved $V_{OC}$. Hence, the improvement in $V_{OC}$ is likely related to the increased D/A interfacial CT-state driven by the wider Y6 bandgap (Figure S1c, Supporting Information) which is demonstrated by the blue shift of Y6 emission (Figure 1b) upon dilution. This is consistent with previous reports that correlate the CT state energy of PM6:Y6 to $V_{OC}$.[48] The enhanced $V_{OC}$ correlates with the suppressed $J_d$ values for increasing PM6 content, in accordance with Equation 1. In terms of responsivity ($R$, see Figure 2c) at reverse bias high values are achieved even for diluted blends, with a maximum of ca. 0.2 A W$^{-1}$ nm$^{-1}$. In the assumption of $J_d$ being

**ADVANCED**
SCIENCE NEWS

www.advancedsciencenews.com

**ADVANCED**
OPTICAL
MATERIALS

www.advopticalmat.de

dominated by the shot noise contribution due to the discrete nature of electric charges,[6] specific detectivity $D^*$ can be calculated as:

$$D^* = \frac{R}{\sqrt{2qJ_d}} \tag{3}$$

here, thanks to the successfully suppressed $J_d$ and despite a lower $R$, diluted BHJ devices give an exceptional $D^*$ with over $5 \times 10^{12}$ Jones ($-4$ V) being achieved in 1:0.1 blends, a $D^*$ 15 times higher than the 1:1.2 blend case (Figure 2d). We note that the $D^*$ value can be overestimated by using equation[3] with only considering shot noise.[53] Therefore, we measured the overall noise current through a low-noise amplifier and performed a fast Fourier transform to obtain the noise spectral density (Figure S7a, Supporting Information). Based on the measured noise current, we then recalculated the corrected specific detectivity $D^*_{corr}$ (Figure S7b, Supporting Information). The $D^*_{corr}$ of the diluted BHJ devices remains above $5 \times 10^{12}$ Jones at $-3$ V, which is five times higher than that of the balanced blend case. These data indicate a significant advantage of the diluted Y6 systems as OPDs, achieving state-of-the-art performances due to strong $J_d$ suppression and large $D^*$ enhancement.

## 2.3. Electric-Field Dependent Photodetector Properties

To understand the origin of device performance enhancement and the impact of blend ratio on the OPD operation mechanisms we turn to the detailed characterization of optoelectronic properties and transient photophysics in PM6:Y6 devices under reverse bias. **Figure 3a,b** shows the effect of reverse bias on the external quantum efficiency (EQE) spectra of the diluted and balanced devices, respectively. The E-field dependent EQE spectra for other blend ratios are presented in Figure S8 (Supporting Information). The spectra span from 300 to 900 nm, showing effective charge generation and collection over the whole absorption range of both PM6 and Y6. The EQE shape is broad for balanced BHJs, but more defined around the PM6 and Y6 absorption peaks in the more diluted blends. At 0 V the diluted 1:0.1 BHJ devices exhibit low EQE (a maximum of 15.9%) but this is strongly increased under reverse bias to ca. 44% at -5 V, with even the Y6 range showing a high EQE of 27%. On the other hand, the balanced blends exhibit a high, almost bias-independent EQE (≈80%). The bias dependence in the diluted blend arises from an enhancement in charge generation and/or extraction across the whole wavelength range, as shown by the minimal changes in EQE spectral shapes upon application of bias (see normalized EQE data in Figure S9, Supporting Information).

To further identify the origin of the photocurrent increase, E-field dependent PL measurements were carried out, Figure 3c,d. We assign PL emission in the blends to CTE emission of Y6, with no measurable emission observed from the polymer. The first thing to note is that the PL at 0 V of the diluted blend is ≈8x higher than the balanced blend despite containing much less acceptor. This indicates that excited states in the balanced blend are efficiently quenched by charge generation at short circuit, consistent with the high EQE observed at 0 V. Upon the application of reverse bias, the PL of the diluted blend is strongly quenched,

while the balanced blend demonstrates only mild quenching. The strong bias dependent PL quenching and EQE increase of the diluted blend can be related to efficient charge generation by field-driven dissociation of the emissive Y6 CTE state. This is supported by transient photocurrent measurements that show a systematic photocurrent increase for diluted blends under increasing reverse bias (Figures S10 and S11, Supporting Information), while little enhancement appears in the balanced case despite higher absolute values.

These results give some important insights into the origin of field-dependent device performance in diluted systems. When small Y6 domains are embedded in the dominant PM6 matrix (i.e., diluted blends), D to A energy transfer is highly efficient even at low Y6 content, evident from only Y6 CTE emission being observed (Figure S2, Supporting Information). The excited state on Y6 is then expected to undergo charge generation by hole transfer from the Y6 to the PM6. This, however, is not the case, with Y6 CTE states being highly emissive and charge generation being limited at short-circuit, resulting in six-fold higher PL emission. Therefore, an additional driving force is required for effective charge generation. This is achieved upon application of a reverse bias, in which PL is quenched and EQE is enhanced, evidence of suppressed radiative recombination due to enhanced charge generation. On the other side, balanced blends demonstrate efficient excited state quenching (low PL) and charge generation (high EQE) without an applied bias. The nature of this charge generation will be discussed in detail below. It is important to note that balanced blend PL is still quenched at increasing reverse bias, as residual CTE states still benefit from electric-field-assisted dissociation. However, the absolute PL yield of these states is very low in highly intermixed BHJs, so that no significant photocurrent gain can be achieved by their separation.

In addition to charge generation and dissociation, the processes of charge transport and extraction also determine OPD performance and should be taken into consideration for a complete picture of device operation. For this purpose, we analyze the photocurrent transients upon pulsed LED excitation (10 Hz), focusing on the fall times of photogenerated signals ($\tau_{fall}$, the time required for the photocurrent to get from 90% to 10% of its initial value upon turn-off). As shown in Figure 3e and Figure S12 (Supporting Information), $\tau_{fall}$ is extremely fast for diluted BHJs, in line with FOMs of state-of-the-art OPDs.[41,54] With no applied bias, a $\tau_{fall}$ of 4.7 µs is observed, compared to 9.0 µs for the balanced blend. This is only slightly improved under reverse bias for the diluted blend, reaching a $\tau_{fall}$ of 4.5 µs at $-2$ V, while the balanced blend shows a marked improvement, achieving a $\tau_{fall}$ of 4.6 µs at $-2$ V (Figure 3f, with all bias conditions shown in Figure S13, Supporting Information). External bias is therefore not critical for fast charge extraction in diluted blends despite being essential for efficient photocurrent output. Oppositely, an electric field is required for fast photoresponse in balanced blends although it is less important for photocurrent generation.
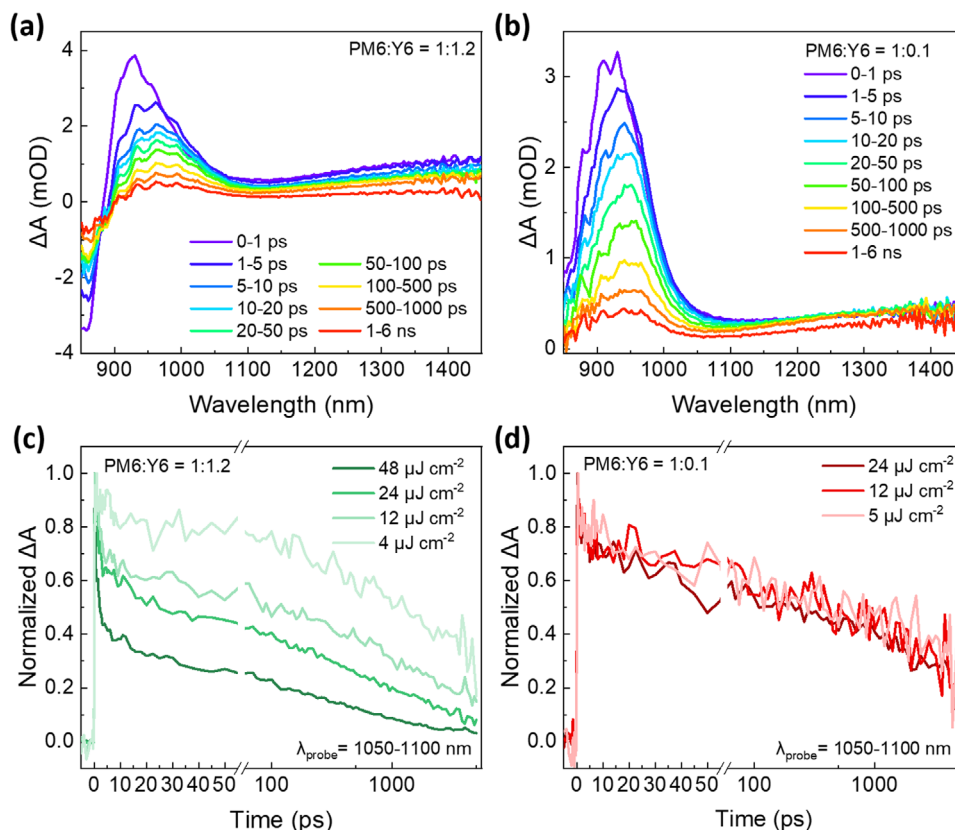
These results give further indications on the photophysical mechanisms responsible for device performance. Efficient charge extraction may only be achieved in the balanced blend with reverse bias due to the high ratio of D/A domain boundaries which can induce traps disrupting charge transport in the
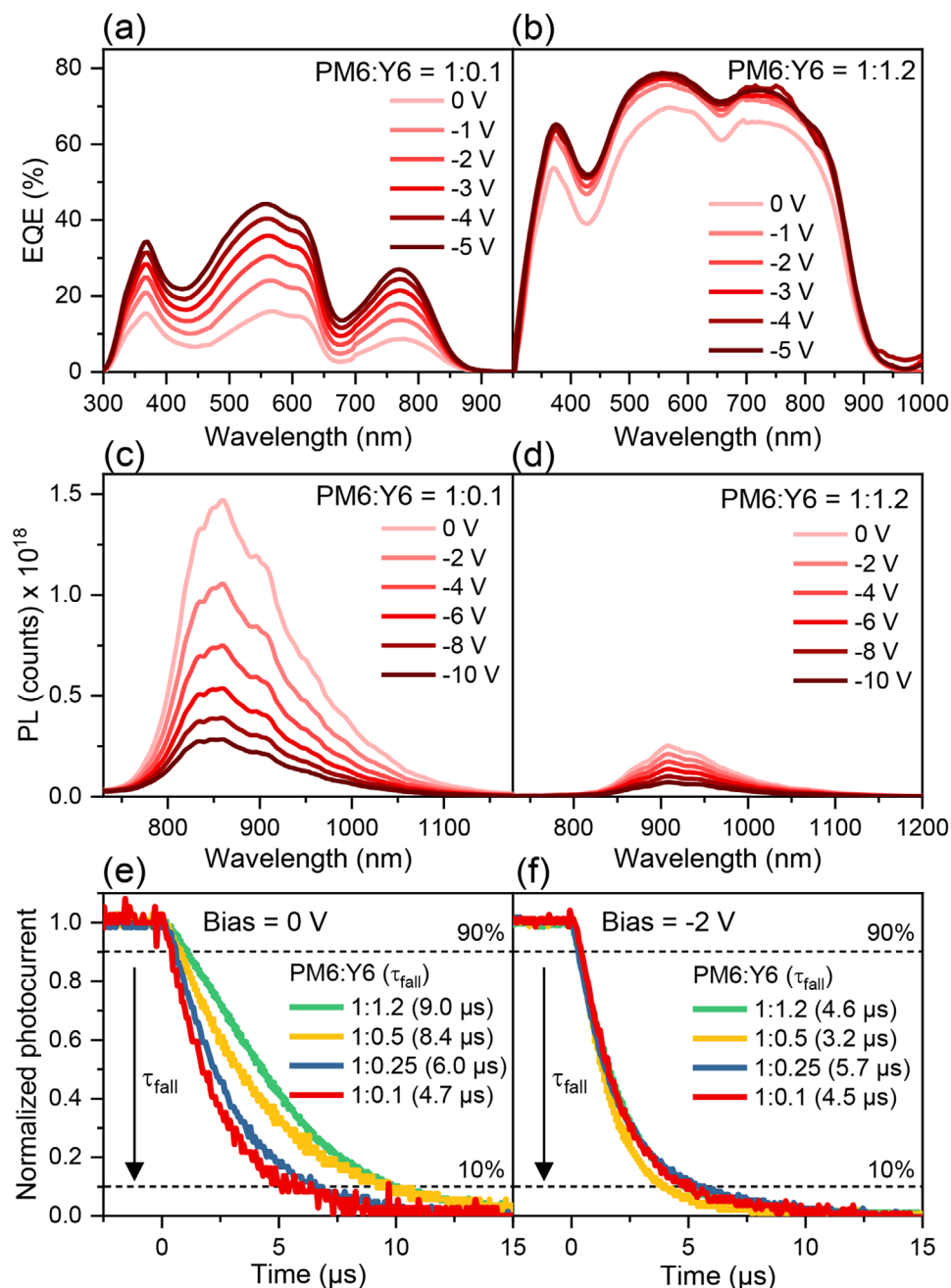
**Figure 3.** Bias dependent characterization of optoelectronic properties in PM6:Y6 devices with different D/A blend ratios. a,b) EQE and c,d) PL spectra under increasing reverse bias for diluted, and balanced BHJ devices. Transient photocurrent decay under f) no bias and f) -2 V condition, with 90% and 10% fall times indicated as dotted line. Decay times $\tau_{fall}$ are indicated in the legend.

highly intermixed system, which we confirm below.[55] In the diluted blend, charge generation is the limiting step, but the polymer matrix and homogeneous morphology, with its limited presence of domain boundaries, enable more effective charge extraction. This is confirmed by the 4 times higher space-charge-limited current (SCLC) hole mobility in diluted blend devices ($8.1 \times 10^{-4}$ cm$^2$ V$^{-1}$ s$^{-1}$), compared to balanced ones ($1.8 \times 10^{-4}$ cm$^2$ V$^{-1}$ s$^{-1}$), as in Figure S14 (Supporting Information). Here, it is interesting to notice that hole transport has the dominant role in determining photoresponse, despite electron mobility being significantly lower. However, PM6 domains are likely to be able to sustain electron transport as well, exemplified by the excellent photoresponse time in PM6-only OPDs (see Figure S12, Supporting Information). In conclusion, inefficient charge generation of donor-rich devices can be improved under reverse bias, which, combined with effective transport, ensures superior OPD performances under mild electric fields.

**ADVANCED**
SCIENCE NEWS

www.advancedsciencenews.com

**ADVANCED**
**OPTICAL**
**MATERIALS**

www.advopticalmat.de

**Figure 4.** Transient absorption spectroscopy. Transient absorption spectra of a) balanced and b) diluted PM6:Y6 BHJ thin films. Fluence-dependent kinetics probed at 1050–1100 nm are shown in (c,d), respectively.
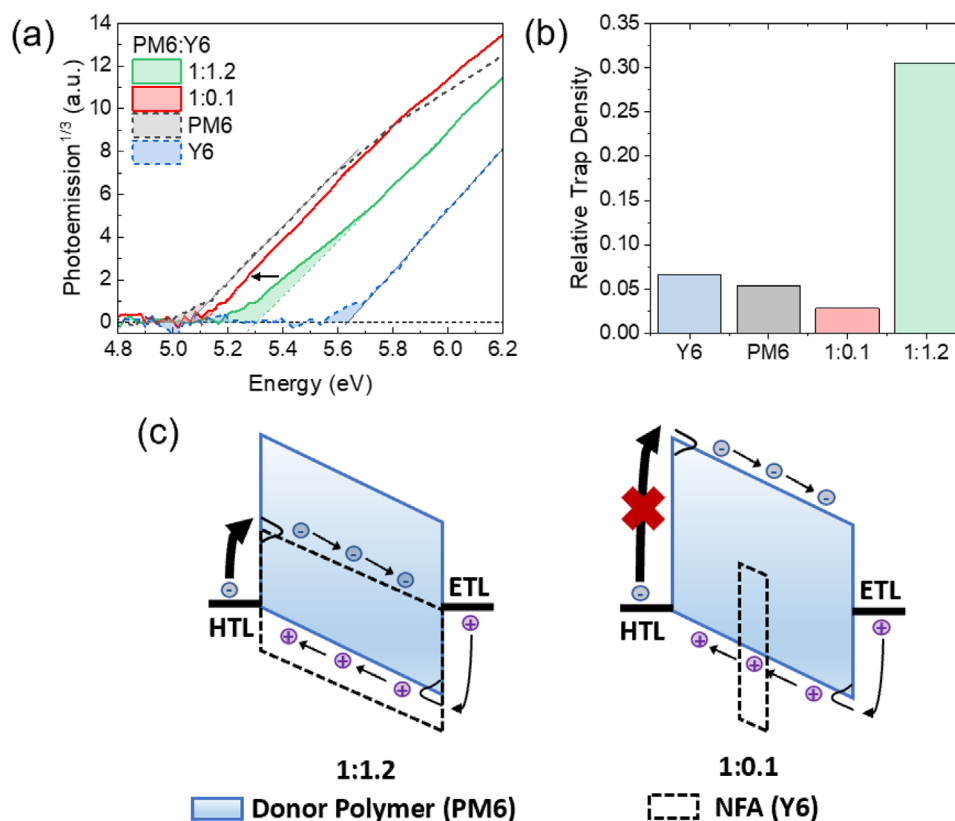
## 2.4. The Nature of Excited States

To gain more insight into the nature of charge generation and dissociation processes, we turn to ultrafast transient absorption spectroscopy (TAS) investigations of BHJ films. As presented in **Figure 4**a,b, the samples are excited at 750 nm, resonant with the Y6 absorption in order to probe charge generation, as effective energy/electron transfer from PM6 to Y6 has already been observed by complete quenching of PM6 emission in blends. Figure 4a shows that the ground state bleach of Y6 is visible below 900 nm, and Y6 photoinduced absorption (PIA) bands appear at 950 and 1350 nm.[56,57] The assignment of these peaks is not trivial, and much discussion is available in the literature.[58] Here, we first consider the PIA at 950 nm. As the pump-probe time delay increases, this PIA shifts to longer-wavelengths in both balanced and diluted blends, as well as in neat Y6 films (Figure S15, Supporting Information), indicative of ultrafast excited state delocalization and the formation of the Y6 CTE states introduced above.[21] The peak shift is more pronounced for the balanced blend, indicating a larger degree of delocalization than in the dilute blend (Figure S16, Supporting Information). Different kinetics at the high (900–920 nm) and low (1050–1100 nm) energy shoulders of the PIA confirm this assignment of multiple Y6 electronic species (Figure S17, Supporting Information).

The excited state decay kinetics are extracted from the low energy shoulder of the peak. Fluence dependent analysis shows a clear distinction between the PIA decay of the balanced and diluted BHJ systems (Figure 4c,d). For the balanced blend, the PIA decay accelerates at higher fluence, while diluted blends demonstrate fluence-independent behavior. This indicates that the excited state bimolecularly decays in the balanced BHJs, and monomolecularly in diluted BHJs. We assign the bimolecular decay of the excited states in balanced blends to exciton–exciton annihilation (and possibly exciton-charge annihilation), as has been observed in neat Y6 films.[21] In the diluted blend the more isolated and less interacting nature of Y6 domains, means that CTE-CTE annihilation is suppressed. Instead, diluted blend excited states (dominated by Y6 CTE states) decay geminately, consistent with the increased emission in these blends despite less acceptor content. This is further supported by the long-lived PL observed in diluted blends (lifetime >5 ns), compared to the very fast decay in balanced BHJs (see transient PL following selective Y6 excitation, Figure S18, Supporting Information).

To investigate the different nature of excited states we also carried out temperature-dependent PL measurements to calculate their binding energy ($E_B$, see Note S1, Supporting Information).[59] The balanced blend shows little PL quenching across the temperature range studied, giving a small $E_B$ energy <10 meV, consistent with previous reports.[15] However, the CTE $E_B$ in the diluted blend is calculated at 180 ± 40 meV, indicating much more strongly bound species. In this context, an external electric field can be expected to have a much stronger effect on dissociation of strongly bound species rather than loosely bound electron-hole pairs. Therefore, field-driven CT separation

**ADVANCED**
SCIENCE NEWS

www.advancedsciencenews.com

**ADVANCED**
OPTICAL
MATERIALS

www.advopticalmat.de

**Figure 5.** Energetic analysis and schematics of BHJ photophysical mechanisms. a) Photoemission spectra of PM6, Y6, and their blends, with the arrow indicating the shift of PM6 HOMO from balanced to diluted blends. b) The extracted tail areas of the photoemission onsets. c) Schematic of dark charge injection under reverse bias in balanced and diluted PM6:Y6 blends.

is likely to be the key to efficient photocurrent generation in diluted BHJs despite limited D/A domain intermixing. At the same time, the strong binding energy of excited species can contribute to low $J_d$, suppressing the thermal component of dark carrier generation.[28]
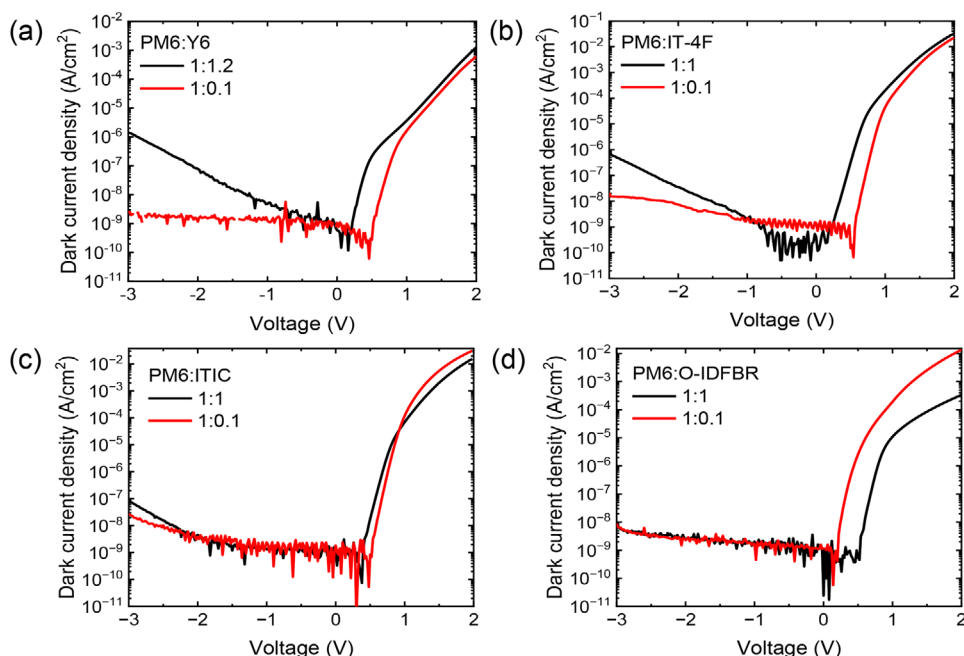
### 2.5. Energetic Landscape upon Acceptor Dilution

To understand charge dissociation in BHJ systems and identify the origin of the low $J_d$, the energetic landscape at the D/A interface was also considered. Initial efficient energy transfer from PM6 to Y6 (Figure 1c) via Förster resonance makes hole transfer to PM6 the main charge generation mechanism, so that the interfacial HOMO offset plays an essential role in device photophysics. Here, we carry out a detailed analysis of BHJ energetics by air photoemission spectroscopy (APS), providing information on HOMO energy levels and the sub-bandgap trap densities.[60] As shown in **Figure 5a** (see Figure S19, Supporting Information, for the full blend series), the photoemission onset in blends arises from the PM6 HOMO (i.e., the shallowest component). With increasing Y6 load, the HOMO level of PM6 is systematically deepened compared to neat PM6 by up to ≈200 mV, reaching -5.25 eV for balanced BHJs. Such deepening can be understood by the strong quadrupole effect of Y6 at D/A interfaces[20] and reduced PM6 crystallinity.[61] Conversely, diluted blends have

a PM6 HOMO of −5.09 eV, much closer to the value for neat PM6. Such a shallower PM6 HOMO level in diluted blends results in a larger HOMO offset at the PM6/Y6 interface compared to balanced counterparts, which would effectively increase the driving force for hole transfer.

The sub-bandgap trap densities of the blends are also compared by the extracted tail areas of photoemission shown in Figure 5b. The neat films and the diluted blend have sharp photoemission onsets and relatively low tail areas, while the balanced blend has a much larger tail state area. This is indicative of a higher trap density in the balanced blend, possibly originating from more intermixed and isolated polymer domains. This may impact the charge collection efficiency, with the higher trap density contributing to the slower photoresponse of the balanced blend devices.

Considering the interfacial energetics at the BHJ/interlayer interface, we can understand the undesirable dark charge injection routes that contribute to the dark current in devices (Figure 5c). In balanced blends, electrons are injected into the Y6 LUMO from the MoO₃ HTL, while holes are injected from the ZnO ETL into the HOMO level of the PM6 polymer. In diluted blends there is little contact area between the interlayers and Y6, inhibiting electron injection into the Y6 LUMO. Instead, electron injection is suppressed as it now requires surmounting the much higher barrier into the lower-lying polymer LUMO. This reduced dark charge injection is a key factor in lowering the $J_d$ in donor-rich

**ADVANCED
SCIENCE NEWS**

www.advancedsciencenews.com

**ADVANCED
OPTICAL
MATERIALS**

www.advopticalmat.de

**Figure 6.** Dark current with various NFAs. Dark J-V curves of balanced and diluted (ratios of donors: acceptors are given in the legend) OPD devices utilizing PM6 with a) Y6, b) IT-4F, c) ITIC, and d) O-IDFBR.

BHJs. Dark injection is also inhibited by the lower number of trap states in the diluted blend, as sub-gap states can provide a lower barrier for charge injection. Additionally, the thermal contribution to $J_d$ is suppressed by the wider Y6 optical bandgap in the diluted blend. Together, these three factors rationalize the extremely low $J_d$ for donor-rich BHJs.

## 2.6. Generality of Approach

OPD devices were fabricated with a range of diluted acceptor blends to assess the generality of our approach. We fabricated PM6 BHJ OPV devices with IT-4F, ITIC, and O-IDFBR. The $J_d$ of the balanced and diluted devices of these blends are shown in **Figure 6**. The improvement in dark current upon dilution is largest for Y6, smaller for IT-4F, even less for ITIC, and negligible for O-IDFBR which shows a very low dark current even in balanced blends (**Figure 7a**). This trend in dark current improvement corresponds to the enhancement of OPD detectivity (Figure S20, Supporting Information), where the order is Y6 > IT-4F > ITIC, whereas the O-IDFBR diluted blends exhibits lower detectivity than the balanced case due to poor charge generation. The efficacy of the dilution strategy, therefore, depends on the choice of acceptor.

To first understand the impact of the acceptors on dark current in the balanced blends, we consider the role of these acceptors in changing the energetic landscape within devices with the acceptor LUMO levels and optical bandgaps (Figure S21, Supporting Information) plotted with the dark current of balanced blends in Figure 7b. Y6 and IT-4F have similarly deep LUMO levels, while ITIC's is shallower, and O-IDFBR's is the shallowest. A shallower LUMO level results in a higher barrier for dark electron injection from the HTL, so the balanced blends of ITIC and O-IDFBR ex-

hibit a lower dark current due to this increased barrier. In terms of thermal generation, the optical band gap of the acceptor is the important factor with a lower bandgap resulting in more thermal generation. The optical bandgap trend is Y6 < IT-4F < ITIC < O-IDFBR, which inversely correlates to the trend in dark current in the balanced blends. These energetic trends explain the trend in balanced blend dark current. By managing dark injection through barrier heights and thermal contributions, we demonstrate it is possible to lower the dark current in balanced blends, although our dilution strategy is more effective with the best performance coming from diluted PM6:Y6.

The efficacy of the dilution strategy is best demonstrated by the ratio of dark current in the balanced and dilute blends as shown in Figure 7c. To understand this trend, it is necessary to consider the nature of the acceptors. Y6, is highly crystalline in the solid state driven by strong intermolecular interactions, IT-4F is less crystalline, but has stronger intermolecular interactions than ITIC,[62] while the twisted geometry of O-IDFBR shows poor aggregation in the solid state and weak intermolecular interactions.[63] Upon dilution, each acceptor shows a blue shift of the absorption peak (Figure S22, Supporting Information) and an increase in optical bandgap, with the degree of this shift following Y6 > IT-4F > ITIC > O-IDFBR. This blueshift in bandgap results in a reduced thermal contribution to dark current but is also demonstrative of disrupting the intermolecular interactions of the acceptors. The trend aligns with the observed reduction in $J_d$ (Figure 7c), suggesting that the dilution-induced disruption of intermolecular interactions contributes to the reduction of $J_d$. This result highlights that the dilution strategy is best used for the highly crystalline acceptors that exhibit strong intermolecular interactions whose properties are not conducive to achieving a low dark current. This is important as it is these highly crystalline acceptors, particularly the Y6 family,
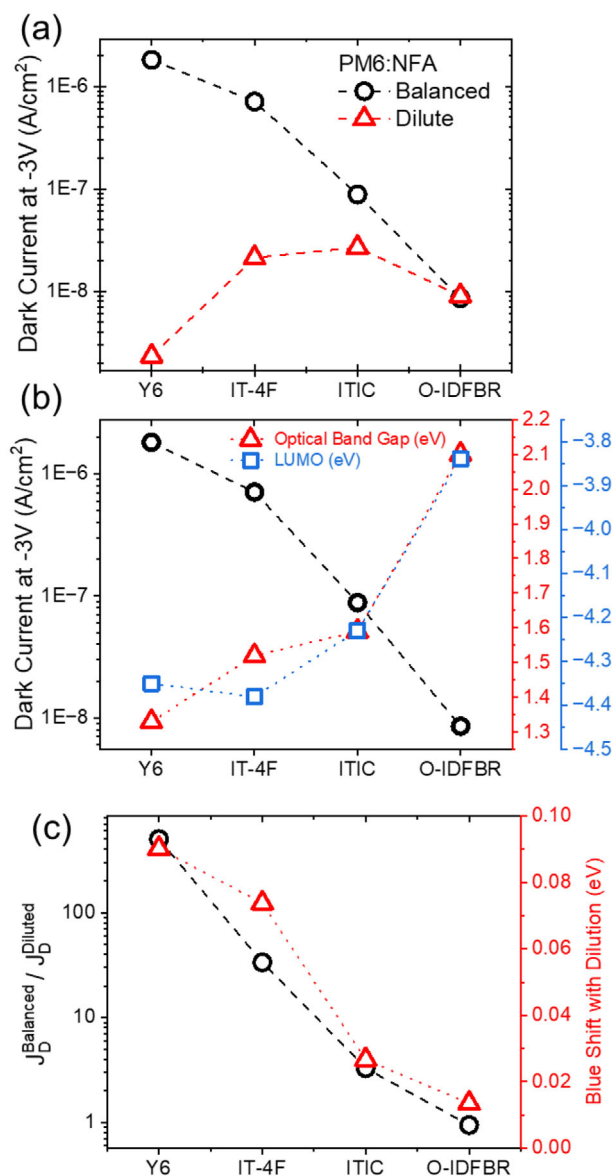
**Figure 7.** Dark current trends with various NFAs. a) Extracted dark current values at -3 V for balanced and diluted OPD devices with different acceptors. b) The dark current of balanced devices with different acceptors at −3 V plotted with LUMO energy levels and optical gaps of the acceptors used. c) The ratio of balanced blend and diluted blend dark current at -3 V plotted with the blue-shift of the acceptor absorption peak upon dilution (see Figure S19, Supporting Information, for details). Lines are used to guide the eye only.

that demonstrate the highest photocurrents and are, therefore, the most promising for OPD applications.

To confirm the important role of the acceptor in the dilution strategy we utilized a different donor polymer J52 (structure shown in Figure S23a, Supporting Information) and fabricated J52:Y6 devices, with the OPD performance and optoelectronic properties of balanced and diluted devices shown in Figure S23 (Supporting Information). As with PM6:Y6, the dark current is significantly lowered in the diluted blends, enhancing detectivity. The optoelectronic properties of the balanced and diluted J52:Y6

blends show the same trends as PM6:Y6. This highlights the key role of the acceptor in determining dark current in these devices and demonstrates the further generality of the dilution strategy.

## 3. Discussion/Conclusions

We have demonstrated the superior OPD performance of diluted acceptor BHJ blends under mild reverse bias. The reverse bias is required due to the different nature of Y6 CTE states in the balanced and diluted blends and the resultant impact on charge generation. In both blends, the majority of charge generation goes via the Y6 CTE state. Initial photoexcitation of PM6 results in rapid energy transfer to the lower bandgap Y6. The excited state on Y6, formed following energy transfer or Y6 photoexcitation, rapidly relaxes to the CTE state formed between strongly coupled Y6 molecules.

In diluted Y6 blends the CTE state is spatially localized and therefore exhibits a strong binding energy. At 0 V these isolated states decay monomolecularly with strong radiative decay observed. It may appear surprising that the CTE state is not effectively quenched by charge separation at the heterointerface with PM6, however the energetic offset at this interface is not large enough to overcome the large $E_B$ of the localized CTE states. Instead, a reverse bias is required to drive charge separation of these CTE states in the diluted blend.

In balanced blends excited states are able to delocalize in the bulk Y6 domains and interact with each other resulting in bimolecular exciton-exciton annihilation. The low $E_B$ of these delocalized excited states means they are easily separated by energetic offsets in the blend, either at the heterointerface with PM6, or as we have seen in neat Y6 at the interface between differently orientated Y6 molecules. In fact, charge generation in neat Y6 is thought to be essential for overall effective charge generation, with the required orientation defined interfaces only being present when sufficiently large Y6 domains are observed, as in the balanced blends.[20] The differences between charge generation in the diluted and balanced blends are detailed schematically in **Figure 8**.

In summary, we present a detailed study of optoelectronic properties and device photophysics of PM6:Y6 systems depending on blend ratio, showing the advantages of polymer rich systems for OPD operation, in which the use of a mild reverse field enables effective charge separation. This photocurrent enhancement combined with the extremely low dark current $J_d$ at high reverse bias results in an excellent detectivity $D^*$ in OPD devices. Additionally, fast charge transport through the polymer matrix ensures a fast photoresponse, crucial for high-frequency photodetection. The generality of this dilution strategy is demonstrated with other NFAs, and is shown to be most effective with highly crystalline acceptors with strong intermolecular interactions. By comparing Y6 with other NFAs, we demonstrate that dark current suppression arises from dilution-induced disruption of NFA crystallinity and intermolecular interactions. These results provide molecular-level insights into the structure–function relationships that govern OPD performance, with broader implications for organic semiconductor research.

Our diluted devices demonstrate a practical approach for achieving state-of-the-art FOMs in solution processed OPDs. This simple strategy removes the need for arduous morphology
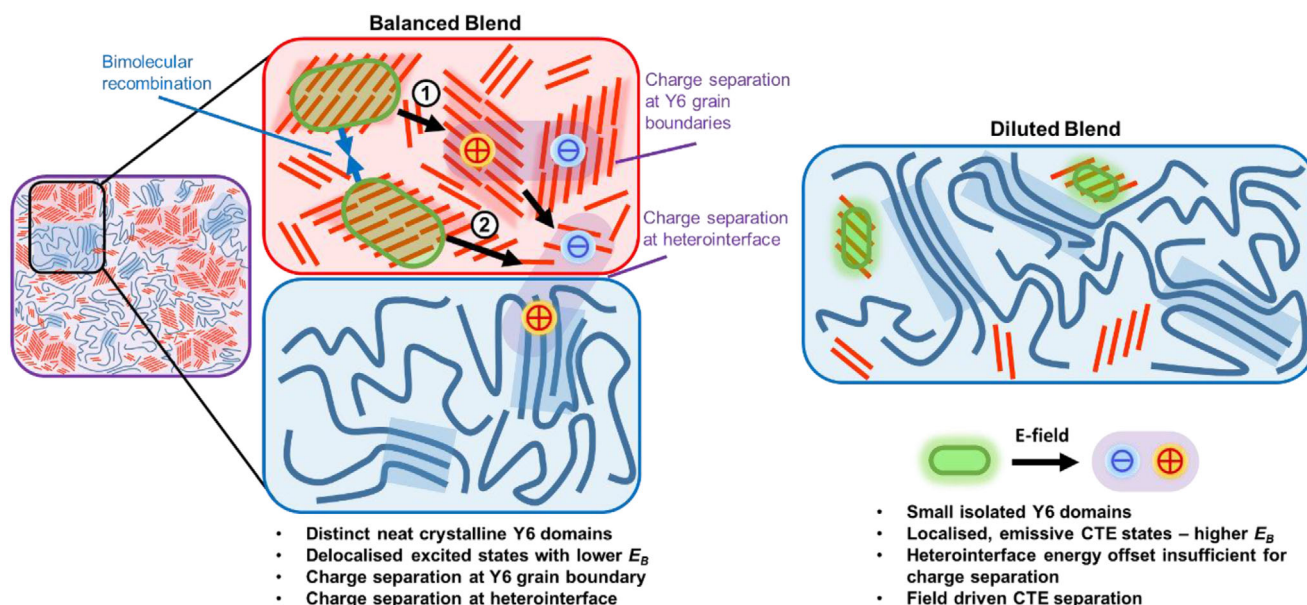
**Figure 8.** Charge generation in balanced and diluted blends. A schematic demonstrating excited state delocalization (green blobs) formation in diluted and balanced blends, and how this affects charge generation in the different blends. Polymer chains are shown in blue, while Y6 molecules are shown in red. Charge separated states are shown in purple, with the electron and holes denoted by negative and positive charges, respectively.

optimization (e.g., thermal treatments, solvent additives) compared to the delicate BHJ engineering for balanced D/A ratios. Additionally, this approach requires no additional fabrication steps or postprocessing, making it cost-effective and easily integrated into existing up-scaling processes. High polymer donor content is also beneficial for the mechanical properties and lifetime of devices making diluted BHJs greatly promising for industrially scalable, stable and highly efficient OPDs. Moreover, our findings demonstrate that blend ratio engineering is a powerful tool to control the nature of photogenerated species and shines light on the unique properties of this high-performing family of Y6 acceptors.

## 4. Experimental Section

*Sample and Device Fabrication*: For preparation of thin films and devices, PM6 and Y6 (Solarmer Materials) were mixed in different blend ratios in chloroform solvent (18 mg mL$^{-1}$), heated at 45 °C overnight for complete dissolution. PM6 was also blended with IT-4F, ITIC, and O-IDFBR at 1:1 and 1:0.1 ratios in chloroform solvent (12 mg mL$^{-1}$) and J52:Y6 was blended at 1:1 and 1:0.1 ratios in chloroform solvent (12 mg mL$^{-1}$). ITO and quartz substrates were cleaned with sequential baths of detergent, water, acetone and 2-propanol (15 min each), followed by drying in oven at 80 °C overnight and O$_2$ plasma ashing before film deposition. For device fabrication, ZnO electron transport layer was prepared by sol-gel method (0.11 g mL$^{-1}$ zinc acetate in methoxyethanol with 3 vol% ethanolamine, sonicated overnight), deposited on ITO substrates by spin-coating (4500 rpm, 1 min), and annealed at 190 °C for 20 min. PM6:Y6 active layer was spin-coated at 2500 rpm for 30 s, achieving a 100–150 nm film thickness measured by Dektak surface profilometer. PM6:IT-4F, PM6:ITIC, PM6:O-IDFBR, and J52:Y6 solutions (1:1 ratio) were spin-coated at 2500 rpm for 30 s, while solutions of these blends at a 1:0.1 ratio were spin-coated at 4000 rpm for 30 s, resulting in films approximately 80–100 nm thick. Device hole extraction layer and top anode were deposited by thermal evaporation in vacuum (10$^{-6}$–10$^{-7}$ mbar),

respectively using MoO$_3$ (10 nm) and Ag (100 nm). Single carrier devices for SCLC measurements were fabricated with similar procedures, using ITO/PEDOT:PSS/BHJ/MoO$_3$/Ag (hole only) and ITO/ZnO/BHJ/ZnO NP/Ag (electron only) structures, with spin-coated PEDOT:PSS and ZnO nanoparticles, and evaporated MoO$_3$ and Ag. Mobility was calculated using Mott-Gurney relationship.

*Optical Characterization*: Transmittance $T$ of thin films was checked by a Shimadzu UV-2550 UV–vis spectrophotometer, and absorbance $A$ was calculated by the relation $A = \log(T_{substrate}/T_{sample})$, with the approximation of no reflectivity. PL spectra were measured by a Renishaw inVia Raman microscope in backscattering configuration, with a 514 nm laser (Argon, Titanium Sapphire lasers). The samples were kept under nitrogen in a custom-designed chamber to reduce degradation effects. Laser spot diameter was of the order of 10 μm, 25% defocused on the sample, and diffracted light was separated by a diffraction grid (300 lines mm$^{-1}$). Bias-dependent PL was measured using a 532 nm laser. Transient PL of thin films on quartz substrates was measured in air by a photoluminescence spectrometer (FLS1000, Edinburgh Instruments), following sample excitation by an 800 nm laser.

*Electrical Characterization*: Device J–V characteristics were measured in inert environment (N$_2$-filled chamber) in dark and under 1 Sun conditions (Newport solar simulator calibrated at 100 mW cm$^{-2}$ by a Si photodiode), using a Keithley 2400 source meter. External quantum efficiency (EQE) measurements were performed by a tungsten halogen lamp coupled with a grating spectrometer (CS260-RG-4-MT-D), using a BK Precision 9110 power supply to control bias voltage. The photocurrent transients were obtained with a DAQ card connected to a Tektronix TDS3032B Oscilloscope, with sample excitation by a 633 nm LED and bias control by a BK Precision 9110 power supply. Energetics of materials on grounded ITO substrates were checked by APS using an APS04 photoemission system (KP Technology) in ambient conditions with a 2 mm gold tip. Measurements were repeated over multiple positions to calculate experimental error. HOMO levels were extracted from the crossing between the linear fit of the photoemission intensity cube root and the zero emission baseline, and DOS was calculated as first derivative from photoemission cube root spectra.

*Transient Absorption Spectroscopy*: Helios spectrometer (Spectra Physics, Newport Corp.) was used to measure the broadband

pump-probe femtosecond TAS and kinetics for thin film samples. Ultrafast laser pulses (750 nm, 100 fs duration) were generated by a 1 kHz Ti:sapphire regenerative amplifier (Solstice, Spectra Physics, Newport Corp.). One portion of the 750 nm pulse was directed to an optical parametric amplifier (TOPAS Prime, Spectra-Physics) and a frequency mixer (Niruvis, Light Conversion) to tune the visible pump pulses at various wavelengths. The pump pulses were modulated at a frequency of 500 Hz by a mechanical chopper. The rest of the 800 nm pulse was routed onto a mechanical delay stage with a 6 ns time window and directed through a non-linear sapphire crystal (sapphire for the visible region and YAG for the NIR region) to generate a white light probe ranging for the visible region from 400 to 1600 nm. The probe pulse was split into two by a neutral density filter. One portion of the probe pulse served as the reference and was directly sent to the fiber-optic coupled multichannel spectrometers (CCD and InGaAs sensors). The rest of the probe pulse together with the pump pulse were focused onto the same spot on the samples with a beam size of around 0.5 mm$^2$ before sending it to the spectrometer. To compensate the fluctuations, the measured spectrum was normalized to the reference spectrum and averaged for several scans to achieve a good signal-to-noise ratio. Data analysis was performed with the commercialized Surface Xplorer software.

## Supporting Information

Supporting Information is available from the Wiley Online Library or from the author.

## Conflict of Interest

The authors declare no conflict of interest.

## Data Availability Statement

The data that support the findings of this study are available from the corresponding author upon reasonable request.

[1] H. Zhu, Y. Shen, Y. Li, J. Tang, *J. Semicond.* **2018**, *39*, 011011.

[2] A. R. Murad, A. Iraqi, S. B. Aziz, S. N. Abdullah, M. A. Brza, *Polymers* **2020**, *12*, 2627.

[3] K. Baeg, M. Binda, D. Natali, M. Caironi, Y. Noh, *Adv. Mater.* **2013**, *25*, 4267.

[4] H. Xu, L. Yin, C. Liu, X. Sheng, N. Zhao, *Adv. Mater.* **2018**, *30*, 1800156.

[5] G. Simone, M. J. Dyson, S. C. J. Meskers, R. A. J. Janssen, G. H. Gelinck, *Adv. Funct. Mater.* **2020**, *30*, 1904205.

[6] J. Kublitski, A. Hofacker, B. K. Boroujeni, J. Benduhn, V. C. Nikolis, C. Kaiser, D. Spoltore, H. Kleemann, A. Fischer, F. Ellinger, K. Vandewal, K. Leo, *Nat. Commun.* **2021**, *12*, 551.

[7] A. Wadsworth, M. Moser, A. Marks, M. S. Little, N. Gasparini, C. J. Brabec, D. Baran, I. McCulloch, *Chem. Soc. Rev.* **2019**, *48*, 1596.

[8] J. Hou, O. Inganäs, R. H. Friend, F. Gao, *Nat. Mater.* **2018**, *17*, 119.

[9] P. Cheng, G. Li, X. Zhan, Y. Yang, *Nat. Photonics* **2018**, *12*, 131.

[10] J. Zhang, H. S. Tan, X. Guo, A. Facchetti, H. Yan, *Nat. Energy* **2018**, *3*, 720.

[11] J. Yuan, Y. Zhang, L. Zhou, C. Zhang, T. Lau, G. Zhang, X. Lu, H. Yip, S. K. So, S. Beaupré, M. Mainville, P. A. Johnson, M. Leclerc, H. Chen, H. Peng, Y. Li, Y. Zou, *Adv. Mater.* **2019**, *31*, 1807577.

[12] H. Chen, *Sci. China Chem.* **2019**, *62*, 403.

[13] J. Yuan, Y. Zhang, L. Zhou, G. Zhang, H.-L. Yip, T.-K. Lau, X. Lu, C. Zhu, H. Peng, P. A. Johnson, M. Leclerc, Y. Cao, J. Ulanski, Y. Li, Y. Zou, *Joule* **2019**, *3*, 1140.

[14] M. B. Price, P. A. Hume, A. Ilina, I. Wagner, R. R. Tamming, K. E. Thorn, W. Jiao, A. Goldingay, P. J. Conaghan, G. Lakhwani, N. J. L. K. Davis, Y. Wang, P. Xue, H. Lu, K. Chen, X. Zhan, J. M. Hodgkiss, *Nat. Commun.* **2022**, *13*, 2827.

[15] L. Perdigón-Toro, H. Zhang, A. Markina, J. Yuan, S. M. Hosseini, C. M. Wolff, G. Zuo, M. Stolterfoht, Y. Zou, F. Gao, D. Andrienko, S. Shoaee, D. Neher, *Adv. Mater.* **2020**, *32*, 1906763.

[16] S. Karuthedath, J. Gorenflot, Y. Firdaus, N. Chaturvedi, C. S. P. De Castro, G. T. Harrison, J. I. Khan, A. Markina, A. H. Balawi, T. A. Dela Peña, W. Liu, R.-Z. Liang, A. Sharma, S. H. K. Paleti, W. Zhang, Y. Lin, E. Alarousu, S. Lopatin, D. H. Anjum, P. M. Beaujuge, S. De Wolf, I. McCulloch, T. D. Anthopoulos, D. Baran, D. Andrienko, F. Laquai, *Nat. Mater.* **2021**, *20*, 378.

[17] W. Zhu, A. P. Spencer, S. Mukherjee, J. M. Alzola, V. K. Sangwan, S. H. Amsterdam, S. M. Swick, L. O. Jones, M. C. Heiber, A. A. Herzing, G. Li, C. L. Stern, D. M. DeLongchamp, K. L. Kohlstedt, M. C. Hersam, G. C. Schatz, M. R. Wasielewski, L. X. Chen, A. Facchetti, T. J. Marks, *J. Am. Chem. Soc.* **2020**, *142*, 14532.

[18] J. Wu, J. Lee, Y. C. Chin, H. Yao, H. Cha, J. Luke, J. Hou, J. S. Kim, J. R. Durrant, *Energy Environ. Sci.* **2020**, *13*, 2422.

[19] S. Karuthedath, S. H. K. Paleti, A. Sharma, H. Yin, C. S. P. De Castro, S. Chen, H. Xu, N. Alshehri, N. Ramos, J. I. Khan, J. Martin, G. Li, F. Laquai, D. Baran, J. Gorenflot, *Adv. Energy Mater.* **2023**, *13*, 2203464.

[20] Y. Fu, T. H. Lee, Y. C. Chin, R. A. Pacalaj, C. Labanti, S. Y. Park, Y. Dong, H. W. Cho, J. Y. Kim, D. Minami, J. R. Durrant, J. S. Kim, *Nat. Commun.* **2023**, *14*, 1870.

[21] S. Y. Park, C. Labanti, R. A. Pacalaj, T. H. Lee, Y. Dong, Y. C. Chin, J. Luke, G. Ryu, D. Minami, S. Yun, J. Il Park, F. Fang, K. B. Park, J. R. Durrant, J. S. Kim, *Adv. Mater.* **2023**, *35*, 2306655.

[22] J. H. Kim, A. Liess, M. Stolte, A. Krause, V. Stepanenko, C. Zhong, D. Bialas, F. Spano, F. Würthner, *Adv. Mater.* **2021**, *33*, 2100582.

[23] Y. Wang, J. Kublitski, S. Xing, F. Dollinger, D. Spoltore, J. Benduhn, K. Leo, *Mater. Horiz.* **2022**, *9*, 220.

[24] Y. Wei, H. Chen, T. Liu, S. Wang, Y. Jiang, Y. Song, J. Zhang, X. Zhang, G. Lu, F. Huang, Z. Wei, H. Huang, *Adv. Funct. Mater.* **2021**, *31*, 2106326.

[25] H. J. Eun, H. Kye, D. Kim, I. S. Jin, J. W. Jung, S. J. Ko, J. Heo, B. G. Kim, J. H. Kim, *ACS Appl. Mater. Interfaces* **2021**, *13*, 11144.

[26] J. Luke, L. Corrêa, J. Rodrigues, J. Martins, M. Daboczi, D. Bagnis, J. S. Kim, *Adv. Energy Mater.* **2021**, *11*, 2003405.

[27] K. Vandewal, J. Widmer, T. Heumueller, C. J. Brabec, M. D. McGehee, K. Leo, M. Riede, A. Salleo, *Adv. Mater.* **2014**, *26*, 3839.

[28] G. Simone, M. J. Dyson, C. H. L. Weijtens, S. C. J. Meskers, R. Coehoorn, R. A. J. Janssen, G. H. Gelinck, *Adv. Opt. Mater.* **2020**, *8*, 1901568.

[29] O. J. Sandberg, C. Kaiser, S. Zeiske, N. Zarrabi, S. Gielen, W. Maes, K. Vandewal, P. Meredith, A. Armin, *Nat. Photonics* **2023**, *17*, 368.

[30] K. Vandewal, S. Himmelberger, A. Salleo, *Macromolecules* **2013**, *46*, 6379.

[31] W. Zhen-Chuan, M.-S. Niu, T. Wang, Z.-H. Chen, J.-J. Guo, C.-C. Qin, L. Feng, H. Yin, X.-T. Hao, *J. Phys. D: Appl. Phys.* **2021**, *54*, 035106.

[32] N. Yao, J. Wang, Z. Chen, Q. Bian, Y. Xia, R. Zhang, J. Zhang, L. Qin, H. Zhu, Y. Zhang, F. Zhang, *J. Phys. Chem. Lett.* **2021**, *12*, 5039.

[33] G. Zhou, M. Zhang, J. Xu, Y. Yang, T. Hao, L. Zhu, L. Zhou, H. Zhu, Y. Zou, G. Wei, Y. Zhang, F. Liu, *Energy Environ. Sci.* **2022**, *15*, 3483.

[34] K. Vandewal, W. D. Oosterbaan, S. Bertho, V. Vrindts, A. Gadisa, L. Lutsen, D. Vanderzande, J. V. Manca, *Appl. Phys. Lett.* **2009**, *95*, 123303.

[35] F. Piersimoni, S. Chambon, K. Vandewal, R. Mens, T. Boonen, A. Gadisa, M. Izquierdo, S. Filippone, B. Ruttens, J. D'Haen, N. Martin, L. Lutsen, D. Vanderzande, P. Adriaensens, J. V. Manca, *J. Phys. Chem. C* **2011**, *115*, 10873.

[36] L. Li, F. Zhang, J. Wang, Q. An, Q. Sun, W. Wang, J. Zhang, F. Teng, *Sci. Rep.* **2015**, *5*, 9181.

[37] Q. Wang, F. Cui, M. Sha, C. Zhang, X. Liao, H. Yin, X. Hao, *Adv. Funct. Mater.* **2023**, *33*, 2304169.

[38] W. Yang, W. Qiu, E. Georgitzikis, E. Simoen, J. Serron, J. Lee, I. Lieberman, D. Cheyns, P. Malinowski, J. Genoe, H. Chen, P. Heremans, *ACS Appl. Mater. Interfaces* **2021**, *13*, 16766.

[39] M. Babics, H. Bristow, W. Zhang, A. Wadsworth, M. Neophytou, N. Gasparini, I. McCulloch, *J. Mater. Chem. C* **2021**, *9*, 2375.

[40] C. Fuentes-Hernandez, W.-F. Chou, T. M. Khan, L. Diniz, J. Lukens, F. A. Larrain, V. A. Rodriguez-Toro, B. Kippelen, *Science* **2020**, *370*, 698.

[41] Y. Yu, C. Liu, Y. Peng, B. Jiang, Y. Su, S. Liu, C. Chen, *Adv. Electron. Mater.* **2022**, *8*, 2200585.

[42] L. Zhu, M. Zhang, W. Zhong, S. Leng, G. Zhou, Y. Zou, X. Su, H. Ding, P. Gu, F. Liu, Y. Zhang, *Energy Environ. Sci.* **2021**, *14*, 4341.

[43] H. Fu, Z. Wang, Y. Sun, *Angew. Chem., Int. Ed.* **2019**, *58*, 4442.

[44] Y. Zhang, Y. Xu, M. J. Ford, F. Li, J. Sun, X. Ling, Y. Wang, J. Gu, J. Yuan, W. Ma, *Adv. Energy Mater.* **2018**, *8*, 1800029.

[45] M. Wang, P. Baek, A. Akbarinejad, D. Barker, J. Travas-Sejdic, *J. Mater. Chem. C* **2019**, *7*, 5534.

[46] P. Bi, F. Zheng, X. Yang, M. Niu, L. Feng, W. Qin, X. Hao, *J. Mater. Chem. A* **2017**, *5*, 12120.

[47] L. Perdigón-Toro, L. Q. Phuong, S. Zeiske, K. Vandewal, A. Armin, S. Shoaee, D. Neher, *ACS Energy Lett.* **2021**, *6*, 557.

[48] C. Cheng, S. Wong, G. LeCroy, S. Schneider, E. Gomez, M. F. Toney, A. Salleo, *Adv. Energy Mater.* **2023**, *13*, 2204297.

[49] K. Vandewal, K. Tvingstedt, A. Gadisa, O. Inganäs, J. V. Manca, *Phys. Rev. B: Condens. Matter Mater. Phys.* **2010**, *81*, 125204.

[50] K. D. Rosenthal, M. P. Hughes, B. R. Luginbuhl, N. A. Ran, A. Karki, S. J. Ko, H. Hu, M. Wang, H. Ade, T. Q. Nguyen, *Adv. Energy Mater.* **2019**, *9*, 1901077.

[51] S. Ryu, N. Y. Ha, Y. H. Ahn, J. Y. Park, S. Lee, *Sci. Rep.* **2021**, *11*, 16781.

[52] H. Hwang, D. H. Sin, C. Park, K. Cho, *Sci. Rep.* **2019**, *9*, 12081.

[53] I. K. Kim, J. H. Jo, B. (Jinwoo) Lee, Y. J. Choi, *Org. Electron.* **2018**, *57*, 89.

[54] N. Strobel, N. Droseros, W. Köntges, M. Seiberlich, M. Pietsch, S. Schlisske, F. Lindheimer, R. R. Schröder, U. Lemmer, M. Pfannmöller, N. Banerji, G. Hernandez-Sosa, *Adv. Mater.* **2020**, *32*, 1908258.

[55] S. Y. Park, C. Labanti, J. Luke, Y. C. Chin, J. S. Kim, *Adv. Energy Mater.* **2022**, *12*, 02103237.

[56] R. Wang, C. Zhang, Q. Li, Z. Zhang, X. Wang, M. Xiao, *J. Am. Chem. Soc.* **2020**, *142*, 12751.

[57] T. H. Lee, Y. Dong, R. A. Pacalaj, S. Y. Park, W. Xu, J. Kim, J. R. Durrant, *Adv. Funct. Mater.* **2022**, *32*, 2208001.

[58] S. Shoaee, H. M. Luong, J. Song, Y. Zou, T. Q. Nguyen, D. Neher, *Adv. Mater.* **2023**, *36*, 2302005.

[59] S. Athanasopoulos, F. Schauer, V. Nádaždy, M. Weiß, F. Kahle, U. Scherf, H. Bässler, A. Köhler, *Adv. Energy Mater.* **2019**, *9*, 1900814.

[60] J. Marin-Beloqui, G. Zhang, J. Guo, J. Shaikh, T. Wohrer, S. M. Hosseini, B. Sun, J. Shipp, A. J. Auty, D. Chekulaev, J. Ye, Y.-C. Chin, M. B. Sullivan, A. J. Mozer, J.-S. Kim, S. Shoaee, T. M. Clarke, *J. Phys. Chem. C* **2022**, *126*, 2708.

[61] H. Cha, G. Fish, J. Luke, A. Alraddadi, H. H. Lee, W. Zhang, Y. Dong, S. Limbu, A. Wadsworth, I. P. Maria, L. Francàs, H. L. Sou, T. Du, J. Kim, M. A. McLachlan, I. McCulloch, J. R. Durrant, *Adv. Energy Mater.* **2019**, *9*, 1901254.

[62] J. Luke, E. J. Yang, Y. Chin, Y. Che, L. Winkler, D. Whatling, C. Labanti, S. Y. Park, J. Kim, *Adv. Energy Mater.* **2022**, *12*, 2201267.

[63] J. Luke, E. M. Speller, A. Wadsworth, M. F. Wyatt, S. Dimitrov, H. K. H. Lee, Z. Li, W. C. Tsoi, I. McCulloch, D. Bagnis, J. R. Durrant, J.-S. Kim, *Adv. Energy Mater.* **2019**, *9*, 1803755.